

Characterizing and Optimizing Qubit Coherence Based on SQUID Geometry


Jochen Braumüller^{1,*}, Leon Ding¹, Antti P. Vepsäläinen¹, Youngkyu Sung¹, Morten Kjaergaard¹,
Tim Menke^{1,2}, Roni Winik¹, David Kim³, Bethany M. Niedzielski³, Alexander Melville³,
Jonilyn L. Yoder³, Cyrus F. Hirjibehedin³, Terry P. Orlando¹, Simon Gustavsson¹ and
William D. Oliver^{1,2,3,4}

¹Research Laboratory of Electronics, Massachusetts Institute of Technology, Cambridge, Massachusetts 02139, USA

²Department of Physics, Massachusetts Institute of Technology, Cambridge, Massachusetts 02139, USA

³MIT Lincoln Laboratory, Lexington, Massachusetts 02421, USA

⁴Department of Electrical Engineering and Computer Science, Massachusetts Institute of Technology, Cambridge, Massachusetts 02139, USA

 (Received 5 March 2020; revised manuscript received 7 May 2020; accepted 8 May 2020; published 29 May 2020)

The dominant source of decoherence in contemporary frequency-tunable superconducting qubits is $1/f$ flux noise. To understand its origin and find ways to minimize its impact, we systematically study flux noise amplitudes in more than 50 flux qubits with varied superconducting quantum interference device (SQUID) geometry parameters and compare our results to a microscopic model of magnetic spin defects located at the interfaces surrounding the SQUID loops. Our data are in agreement with an extension of the previously proposed model, based on numerical simulations of the current distribution in the investigated SQUIDs. Our results and detailed model provide a guide for minimizing the flux noise susceptibility in future circuits.

DOI: [10.1103/PhysRevApplied.13.054079](https://doi.org/10.1103/PhysRevApplied.13.054079)

I. INTRODUCTION

During the last two decades, quantum circuits have enabled several proof-of-principle demonstrations of small quantum algorithms and simulations [1–4]. However, a major roadblock toward scaling superconducting circuits to perform useful computations is the limited qubit coherence [5], restricting run times of algorithms or simulations and creating a large resource overhead in quantum error correction schemes.

With many of the recently implemented circuits relying on frequency-tunable qubits, the dominant source of dephasing in these qubits [4,6] is low-frequency flux noise with a power spectral density (PSD) that is inversely proportional to frequency [7]. Such $1/f$ noise is ubiquitous in condensed matter systems [8] and was observed in the context of Josephson devices more than three decades ago [9,10]. With the advent of superconducting qubits, $1/f$ noise in superconducting quantum interference devices (SQUIDs) has been shown to cause qubit dephasing [11–20] as well as qubit relaxation [21,22]. It was proposed that $1/f$ flux noise in qubits comprising SQUIDs originates from magnetic two-level system defects residing in the oxide layers surrounding the SQUID loops [14]. The model assumes a temperature-activated flipping of

independent electronic spins that are randomly oriented and have a random energy distribution [8], leading to a $1/f$ noise PSD. Oxygen adsorbates were determined to be candidate sources for such spin defects by density functional theory calculations [23] and x-ray spectroscopy [24].

An analytic approximation of this microscopic model has been derived by Bialczak *et al.* [15], yielding an expression for the noise PSD $S(\omega) \propto R/W$, where R is the radius of the SQUID loop and W is the width of the superconducting strip forming the SQUID. Indications of such scaling with wire width have been reported [25], but experiments with superconducting phase qubits could not quantitatively confirm the noise amplitudes predicted by the microscopic model, mostly due to uncertainties in the surface spin density. Furthermore, the formation of spin clusters was proposed in order to reconcile the observed noise levels with the model [26,27]. The origin of $1/f$ noise in SQUIDs has remained an unsolved question.

In this paper, we study $1/f$ flux noise in more than 50 capacitively shunted flux qubits [21] with systematically varied geometric parameters of their SQUID loops. Our data show quantitative agreement with the proposed microscopic model of independent magnetic defects that reside in the interface layers surrounding the SQUIDs. In particular, we demonstrate that the extracted flux noise amplitudes follow the expected trends over a large SQUID parameter regime and in a noise frequency range relevant

*jbraum@mit.edu

to contemporary quantum circuits. We even improve this agreement by introducing a numerical extension to the model, overcoming the limited applicability and accuracy of the analytic approximation [15] for realistic circuit geometries.

II. EXPERIMENTAL SETUP

Our experiment incorporates results from six different samples comprising ten uncoupled capacitively shunted flux qubits [21] each; see Fig. 1. Qubit control and dispersive state readout is performed through individual capacitively coupled $\lambda/4$ waveguide resonators, which are in turn inductively coupled to a common $50\ \Omega$ transmission line. The samples are cooled down to approximately 10 mK in a dilution refrigerator. Microwave transmission through the transmission line is used to projectively measure the qubit state with a heterodyne detection scheme at room temperature. Details on sample fabrication are provided in Appendix A.

With the Hamiltonian of each flux qubit nominally identical, we vary the geometric parameters of their SQUIDs as illustrated in Fig. 1(d). While the thickness $b = 190\ \text{nm}$ of the bilayer aluminum film is fixed, the side lengths X and Y , referenced to the inner circumference, and the wire width W are varied. In order to reduce systematic errors, each SQUID variant is represented twice within a chip, resulting in five distinct SQUID geometries per chip. The ranges of the parameter variations are centered around state-of-the-art values used in high-coherence flux qubits [21], $X = 9\ \mu\text{m}$, $Y = 8\ \mu\text{m}$, and $W = 1\ \mu\text{m}$. In Fig. 1(e) we show the effective circuit schematic for one qubit-resonator pair coupled to the common transmission line. Circuit parameters are summarized in Appendix B.

A global external flux bias Φ is applied to the SQUID loops with a coil located in the lid of the sample package.

III. MEASUREMENT TECHNIQUE

We perform noise spectroscopy for every qubit using a sequence of measurements first demonstrated in Ref. [12]. We first extract the qubit spectrum around the optimal bias point at $\Phi = \Phi_0/2$; see Fig. 2(a). Subsequently, we perform a spin-echo experiment, where a π pulse in the middle of a Ramsey sequence inverts the sign of the phase accrual rate due to quasi-static low-frequency noise. As shown in Fig. 2(b), we observe an exponential decay function at the sweet spot, where decoherence is relaxation limited. Further away from the sweet spot, the decay function is predominantly Gaussian, indicative of pure dephasing due to $1/f$ noise [12,28]. The Gaussian pure dephasing rate takes the form $\Gamma_\phi^E = \sqrt{A_\Phi \ln 2} |\partial\omega/\partial\Phi|$ for the echo experiment, assuming Gaussian statistics of the qubit phase accumulation [28] and a noise PSD $S_\Phi(\omega) = A_\Phi/|\omega|$ with noise amplitude $\sqrt{A_\Phi}$. To find the exponential decay rate Γ_{exp} and Gaussian dephasing rate Γ_ϕ^E , we perform a fit to the decay function $p(t) \propto \exp[-\Gamma_{\text{exp}}t - (\Gamma_\phi^E t)^2]$ [12] for each flux bias point. For the individual fits, Γ_{exp} is kept a free parameter with an initial guess of $(2T_1)^{-1}$, as extracted in a preceding relaxation measurement. In order to numerically extract the slope of the spectrum, we fit the hyperbola $\hbar\omega(\Phi) = \sqrt{\Delta^2 + \epsilon(\Phi)^2}$ to the data in Fig. 2(a), which is a good approximation over the measured range close to the sweet spot [21].

In Fig. 2(c) we show the pure dephasing rate Γ_ϕ^E as a function of the slope $(2\pi)^{-1}\partial\omega/\partial\Phi$ of the spectrum for

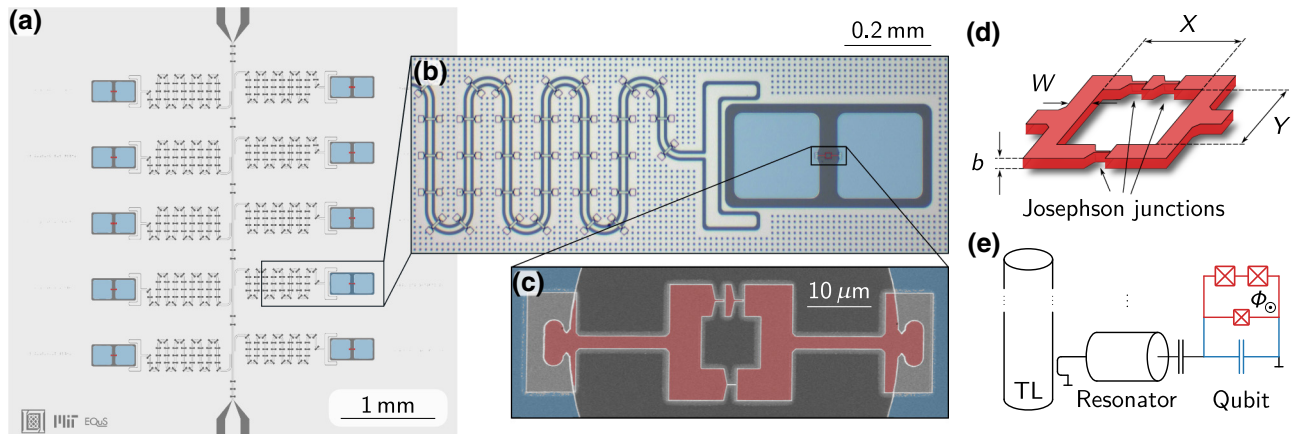


FIG. 1. Noise spectroscopy device. (a) Each chip holds ten uncoupled capacitively shunted flux qubits with individual readout resonators, featuring five different SQUID loop variations at a two-fold redundancy. (b) Optical micrograph of one of the qubits and part of its readout resonator. The capacitive shunt is colored in blue. (c) Electron microscope image of a fabricated SQUID loop. (d) Schematic representation of the SQUID parameters varied across different designs. The SQUID dimensions X , Y are measured along the inner edge of the SQUID, W is the width of the superconducting leads, and b is the film thickness. (e) Effective schematic for one qubit-resonator pair coupled to the common transmission line (TL).

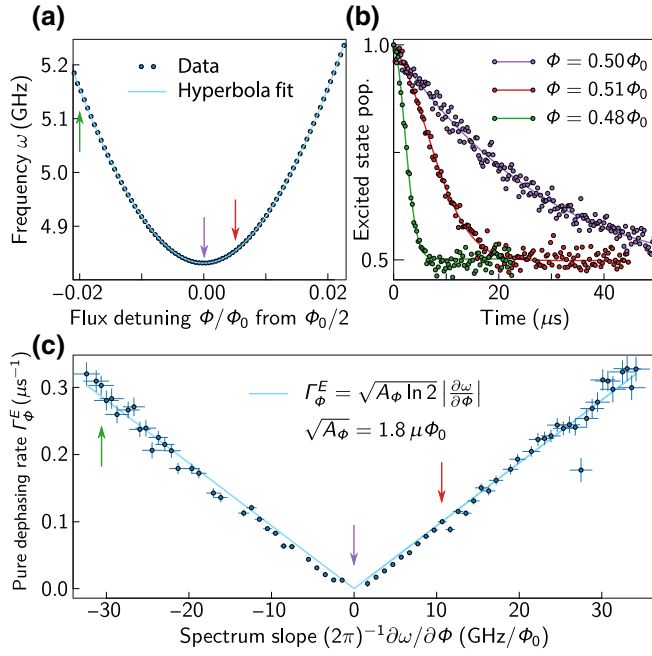


FIG. 2. Experimental technique used for noise spectroscopy. (a) Qubit spectrum around its flux sweet spot at $\Phi = \Phi_0/2$. A hyperbolic fit enables us to numerically extract the slope $(2\pi)^{-1}\partial\omega/\partial\Phi$ of the spectrum. (b) Spin-echo dephasing traces at three illustrative locations of the spectrum (indicated by the arrows). The vertical axis shows the excited state population. (c) By plotting the extracted pure dephasing rates Γ_ϕ^E as a function of the spectrum slope, we can extract the $1/f$ flux noise amplitude $\sqrt{A_\phi}$ from a linear fit.

one of the measured qubits. We perform two separate linear fits (for positive and negative slopes) and extract the noise amplitude $\sqrt{A_\phi}$ and its uncertainty from an error-weighted average. Since pure dephasing in the Gaussian approximation vanishes at the sweet spot, we enforce an intercept with the origin. About 20% of the qubits show a bending of data points to a finite (positive) dephasing rate near the sweet spot. We attribute these deviations to other higher-frequency dephasing processes, which do not significantly compromise the extracted noise amplitudes. The validity of our experimental procedure is limited to a noise PSD $S(\omega) \propto \omega^{-\alpha}$ with $\alpha = 1$; see Appendix C. While $1/f$ noise has been observed with a scaling where $\alpha \leq 1$ [7,8,29,30], this assumption is compatible with previous experiments extrapolated to approximately 10 mK [27] and is supported by the Gaussian decay function we observe in our experiment.

IV. RESULTS

In Fig. 3 we show the measured flux noise amplitudes $\sqrt{A_\phi}$ as a function of SQUID geometry. We categorize the design variations into two groups. Qubits in the first group have SQUID loops with a constant wire width $W =$

$1 \mu\text{m}$ but varying perimeters $21 \mu\text{m} \leq P \leq 101 \mu\text{m}$; see Fig. 3(a). We define the perimeter $P = 2X + 2Y + 4W$, measured along the centerline of the SQUID. The second group of measured qubits have SQUID loops with a fixed inner perimeter $2X + 2Y = 34 \mu\text{m}$ and varying wire width $0.4 \mu\text{m} \leq W \leq 5 \mu\text{m}$; see Fig. 3(b). These subcategories can be understood as line cuts in the two-dimensional parameter space $\sqrt{A_\phi}(P, W)$, given in Fig. 3(c). Measured data show an approximately linear dependence of the noise power A_ϕ on SQUID perimeter P [Fig. 3(a)] and on the inverse wire width W [Fig. 3(b)]. By investigating SQUID loops of varying aspect ratio X/Y , we are able to confirm

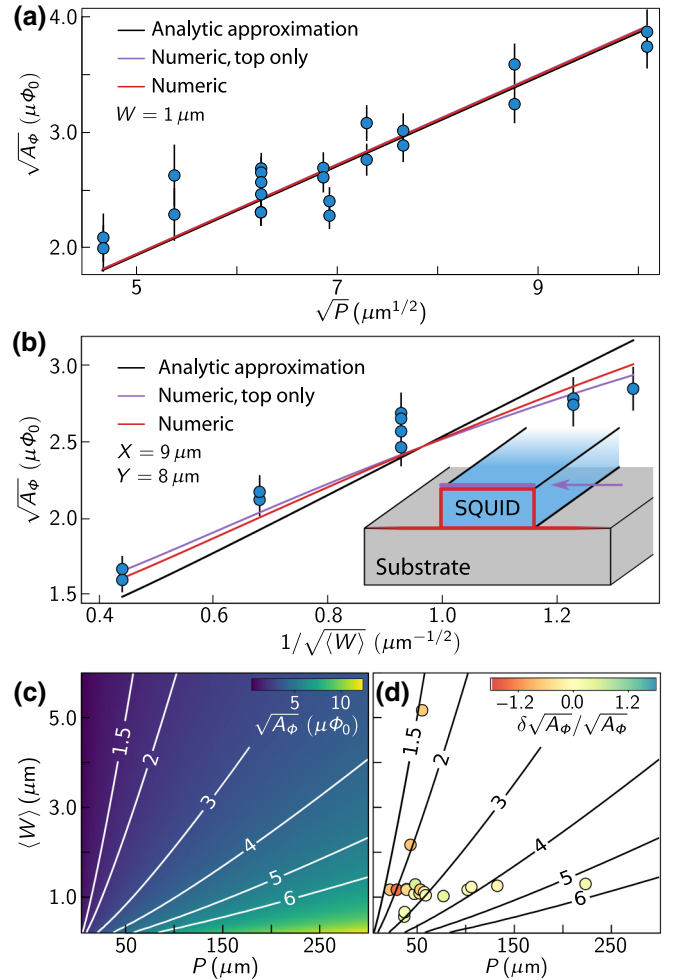


FIG. 3. Flux noise amplitudes $\sqrt{A_\phi}$ as a function of SQUID geometry parameters for (a) constant wire width W and (b) constant inner perimeter $2X + 2Y$. Each line corresponds to an independent fit in this two-dimensional parameter space to the analytic approximation (black line) and numeric variations (purple and red lines) of the model (see the inset). (c) The $\sqrt{A_\phi}$ as a function of the effective width (W) and perimeter P based on a fit to the numeric model taking into account all relevant interfaces [red lines in (a) and (b)]. (d) Data points show experimentally investigated parameter combinations with relative deviations from the same numerical model color coded.

the linear scaling of A_Φ with SQUID perimeter rather than its area.

We compare our experimental data with a model that assumes $1/f$ flux noise to originate from local magnetic two-level system defects residing in the interface layers surrounding the qubit SQUID loops. This model had been proposed previously [14,15], but has eluded quantitative experimental verification. The model assumes noninteracting magnetic defects of areal density σ and with an average magnetic moment m , undergoing a thermally activated, uncorrelated flipping of their spin direction and thereby creating flux noise in the SQUID loop, ultimately leading to qubit decoherence. Modified to the rectangular geometry of the SQUIDs used in our experiment (see Fig. 1) the total flux variance $\langle \Phi^2 \rangle$ in the SQUID is

$$\langle \Phi^2 \rangle = \frac{1}{3} m^2 \sigma P \int dx \left(\frac{B(x)}{I} \right)^2, \quad (1)$$

where m is the magnetic moment of a single spin defect and B is the magnetic field induced by the persistent current I in the SQUID. The integration is carried out perpendicular to the current flow in the SQUID arms within the considered interfaces hosting defects. Previously, an analytic approximation of Eq. (1) was derived [15], modeling the SQUID as two dimensional and assuming a surface current density $K(x) \propto 1/\sqrt{1 - (2x/W)^2} \propto B(x)$ [31] for $-W/2 < x < W/2$, taking into account defects from only the top surface of the SQUID, and yielding

$$\langle \Phi^2 \rangle = \frac{\mu_0^2}{3\pi} m^2 \sigma \frac{P}{W} \left(\frac{\ln(2bW/\lambda^2)}{2\pi} + \frac{e-1}{2\pi} \right), \quad (2)$$

with λ denoting the superconducting penetration depth of aluminum. See Appendix D for a derivation of Eq. (2).

The scaling of flux noise with loop perimeter P can be intuitively understood, since the total number of magnetic defects increases proportionally. The inverse scaling with wire width W is less intuitive, given the increased number of participating defects for wider wires. It can be motivated by the following picture. For a constant persistent current in the SQUID, the magnetic field is diluted across more defect spins residing in the interfaces when increasing the wire width. Since the defects are uncorrelated, their contribution to the total flux noise partially cancels, resulting in an effective decrease of the total flux noise. Independent of the geometry, a uniform current density across the width of the SQUID arms minimizes the flux noise amplitude [32]. This provides an explanation for the previous observation that the presence of a superconducting ground plane reduces flux noise [25,33].

In order to connect the noise amplitude $\sqrt{A_\Phi}$ extracted from measured data with the above model, we use $\langle \Phi^2 \rangle = \int_{-\infty}^{\infty} d\omega S_\Phi(\omega) g_E(\omega) = 2A_\Phi \ln 2$. To account only for frequencies our echo experiment is sensitive to, the

integration is weighted by its filter function g_E ; see Appendix C.

Both black lines in Figs. 3(a) and 3(b) belong to the same two-dimensional fit to the analytic approximation [Eq. (2)] using only a single fit parameter $m^2\sigma$. Rather than relying on a defect density reported in previous calculations or experiments, we are therefore able to extract its value from our experimental data. Assuming a penetration depth of $\lambda = 40$ nm [34] and that the magnetic moment corresponds to a Bohr magneton, $m = \mu_B$, we recover a surface spin density $\sigma = 1.2 \times 10^{17} \text{ m}^{-2}$, a factor of four off the previously predicted [14] and observed [26] value of $5 \times 10^{17} \text{ m}^{-2}$. With an effective spin magnetic moment of $1.8\mu_B$, as suggested for defects formed by oxygen adsorbates on the SQUID surface [23], we extract $\sigma = 3.7 \times 10^{16} \text{ m}^{-2}$.

Because of an offset between the bottom and top metallizations in the shadow evaporation process, the width along the vertical arms of the SQUIDs is increased. This effect is most pronounced in SQUIDs with small aspect ratios ($X \ll Y$) and thin wires. In order to account for this changing width in the SQUID loops, we plot an average width $\langle W \rangle$ in Figs. 3(b)–3(d).

The analytic approximation of the model Eq. (2) is only valid in the regime where $b \sim \lambda$ and $W \gg \lambda$, but in our experiment, $b/\lambda \approx 5$. We attribute the deviations of data points in Fig. 3(b) from the linear scaling for thin wires (largest $1/\langle W \rangle$) to a partial breakdown of the approximate variant of the model. We extend the model by numerically computing the volume current density in the investigated SQUIDs, thereby overcoming the limitations of the analytic approximation. In our numerical approach, the arms of the SQUIDs are modeled as long superconducting strips, which are discretized into parallel sections. The currents in each segment are calculated based on the two-fluid model of superconductivity, where the supercurrent contribution is described through London's equation [35,36]. Subsequently, we can calculate the magnetic field in the various interfaces surrounding the SQUIDs (where magnetic defects reside) with Biot-Savart's formula, replacing the integral in Eq. (1); see Appendix D 2.

Fits to the model with our numerical extension are shown by the purple and red lines in Figs. 3(a) and 3(b). We find quantitative agreement with experimental data, including SQUIDs with small wire widths, where the numeric model is consistent with deviations from the linear behavior, as observed in the experiment. For direct comparison with the analytic approximation, we show the numerical model only including the aluminum-vacuum surface on top of the SQUID (red). We validate our theoretical model by observing good agreement with the analytic approximation for a small film thickness $b \sim \lambda$ and we confirm that the analytic approximation is inaccurate for our film thickness of $b = 190$ nm and breaks down completely for even higher film thicknesses. Based on our numerical results,

we find that increasing the film thickness b decreases the flux noise amplitude, which is analogous to the effect we observe for increasing the wire width W .

In addition, we perform a fit to the numeric model including defect spins residing in all relevant interfaces surrounding the SQUID; see the regions colored red in the inset schematic of Fig. 3(b), i.e., the top and side aluminum-vacuum interfaces, the bottom silicon-aluminum interface, and the silicon-vacuum interfaces beside the SQUID arms, where the magnetic field decays with a power law. Assuming that $m = \mu_B$, we obtain $\sigma = 2.6 \times 10^{17} \text{ m}^{-2}$ when considering only the top surface of the SQUID and $\sigma = 6.7 \times 10^{16} \text{ m}^{-2}$ when including all relevant interfaces with equal defect densities. We performed an alternative fit to measured data assuming different defect densities for the aluminum-vacuum, silicon-vacuum, and silicon-aluminum interfaces based on their extracted loss tangents [37,38], yielding a defect density in the aluminum-vacuum interface of $1 \times 10^{17} \text{ m}^{-2}$.

The two-dimensional fit to our numerical model including all relevant interfaces is depicted in Fig. 3(c), with measured data points shown in Fig. 3(d) and relative deviations from the model color coded. While we measure time-averaged T_1 times in our qubits between 5 μs and 65 μs , with most data points around 20 μs , the extracted values of the noise amplitudes $\sqrt{A_\Phi}$ are in excellent agreement across all measured samples, demonstrating the robustness of our analysis. Dephasing times T_2 are limited by $2T_1$ at the sweet spot and are reduced to approximately 1 μs for the largest frequency detuning from the sweet spot, while T_1 times are not limited by flux noise in these samples. Based on the spin-echo filter function, our experiment is sensitive to noise frequencies in the range of 10 kHz to 1 MHz. The flux bias line used in our experiment is low-pass filtered with a second-order RC filter located at the 3 K stage of the cryostat. In the frequency range relevant to our experiment, we estimate the added flux noise of our setup to be at least two orders of magnitude lower than measured flux noise values, and therefore negligible. Additionally, flux noise that is caused by fluctuations in the bias voltage scales the noise amplitude as $\sqrt{A_\Phi} \propto \sqrt{\langle \Phi^2 \rangle} \propto B \cdot X \cdot Y \propto P^2$, where B is the induced magnetic field in the SQUID. Since this is a different scaling than experimentally observed, we conclude that noise from the current source is insignificant for our experiment.

The noise amplitudes extracted in our experiment are similar to previous observations in phase qubits and flux qubits sensitive to noise frequencies below 1 Hz [15,25]. Since our experiment combines the results of a large number of SQUID loops with geometry parameters distributed in a two-dimensional parameter space, the product of interface defect density and their coupling strength is a single fit

parameter in our analysis. The quantitative agreement we observe between experimental data and microscopic model therefore does not rely on a literature value for the defect density, but rather we are able to extract it from our data set. Given the good agreement with the recently reported value, our experiment provides additional evidence for its accuracy.

Finally, we measure flux noise amplitudes of nine identical qubits with geometry parameters in the optimal limit according to our previous findings. The SQUIDS have small loop perimeters $P = 32 \mu\text{m}$ and increased wire widths $W = 2 \mu\text{m}$. These parameters ensure that the three Josephson junctions can be integrated into the SQUID loop without compromising the fabrication quality, although even smaller P/W may be feasible. For the optimized samples, we find consistently low noise amplitudes with a mean of 1.64 $\mu\Phi_0$ and a standard deviation of 0.11 $\mu\Phi_0$. This verifies the model over a large parameter range and confirms that significant improvements in flux noise levels can be achieved by optimizing SQUID geometry. A summary of the data underlying the results in this paper is provided in the Supplemental Material [39].

The results presented in this paper are not limited to the specific variant of flux qubit used, but are general to any SQUID used in the framework of superconducting circuits. We substantiate this by measurements of $1/f$ flux noise in capacitively shunted flux qubits where the capacitor is formed by a single floating pad that couples to ground, similar to the ‘‘Xmon’’ layout [6]. Both qubit architectures yield consistent flux noise amplitudes for identical SQUID loop geometries.

V. CONCLUSIONS

To conclude, we experimentally demonstrate an approximately linear dependence of the noise power on the SQUID perimeter and inverse wire width. We observe quantitative agreement of our data with an extension of a previously proposed model for magnetic defects residing in material interfaces. Our refined model is based on simulating the current distribution in the SQUID loops, resolving the limited applicability and accuracy of the analytic approximation considered previously. This is an important contribution towards solving the long-standing puzzle surrounding the origin of $1/f$ flux noise in conductors. The obtained results are expected to be universal for any SQUID-based superconducting circuit. The observed trends—namely wide wires, small perimeter SQUIDS, and large thickness films being favorable to suppress flux noise—can therefore serve as a guide to reduce the noise susceptibility of superconducting circuits. In the context of quantum information, this has a direct relevance for improving operational fidelities in both gate-model and quantum annealing approaches to quantum computing.

ACKNOWLEDGMENTS

The authors are grateful to A. Di Paolo and S. Weber for insightful discussions. This research was funded in part by the Office of the Director of National Intelligence (ODNI), Intelligence Advanced Research Projects Activity (IARPA), and the Department of Defense (DoD) via MIT Lincoln Laboratory under Air Force Contract No. FA8721-05-C-0002. The views and conclusions contained herein are those of the authors and should not be interpreted as necessarily representing the official policies or endorsements, either expressed or implied, of the ODNI, IARPA, the DoD, or the U.S. Government.

J.B. and L.D. contributed equally to this work.

APPENDIX A: SAMPLE FABRICATION

The samples are fabricated on a silicon substrate by dry etching an MBE grown, 250 nm thick aluminum film in an optical lithography process and then diced into 5×5 mm² chips. In Fig. 1(b) in the main text we show one of the qubits with its two floating capacitor pads colored in blue. The SQUIDs colored in red in Fig. 1(c) in the main text are fabricated with an electron beam lithography process and a double angle shadow evaporation technique [40] to form the Josephson junctions. Across the entire area of the SQUIDs we evaporate 40 nm and 150 nm thick aluminum films, separated by an oxide layer created with a controlled *in-situ* oxidation. In addition to the desired Josephson junctions, this step also creates a large parasitic oxide layer between the aluminum films, which has been shown to host electric two-level systems that lead to qubit decoherence [41].

APPENDIX B: CIRCUIT PARAMETERS

A schematic of one qubit-resonator pair coupled to the common transmission line is shown in Fig. 1(e) in the main text. The flux qubit consists of a small Josephson junction that is connected in parallel with two larger Josephson junctions with a relative area ratio of 0.42. We observe a mean qubit transition frequency of $\omega/2\pi = 4.6$ GHz and a qubit anharmonicity of approximately 480 MHz at the qubit sweet spot, located at a flux bias Φ corresponding to odd integer multiples of half-flux-quantum $\Phi_0/2$, where $\Phi_0 \equiv h/2e$. We explain the observed standard deviation of 400 MHz in the sweet spot qubit frequencies in part by geometry-dependent variations in the kinetic inductances of the SQUID loops, which are caused by the aforementioned additional parasitic Josephson junctions that form as a result of the shadow evaporation fabrication technique. Additionally, we attribute variations in the qubit transition frequency to a varying junction barrier transparency and small deviations in the junction area. The qubits have a shunt capacitance of 56 fF and a critical current density of

$2.4 \mu\text{A}/\mu\text{m}^2$, resulting in $E_J/h = 36$ GHz for the small Josephson junction.

APPENDIX C: ECHO PURE DEPHASING RATE DUE TO $1/f$ FLUX NOISE

The qubit is described by the Hamiltonian $\hat{H} = \hbar [\omega_0 + \omega(t)] \hat{\sigma}_z/2$, where ω_0 describes a static offset of the qubit frequency and $\omega(t)$ is a stochastic frequency fluctuation induced by flux noise. The solution to the Schrödinger equation $i\hbar(\partial/\partial t) |\psi\rangle = \hat{H} |\psi\rangle$ is

$$|\psi(t)\rangle = e^{i\phi(t)} |\psi(0)\rangle = e^{i\phi_0 + i\varphi(t)} |\psi(0)\rangle, \quad (\text{C1})$$

$$\phi(t) = \omega_0 t + \int_0^t dt' \omega(t'). \quad (\text{C2})$$

We therefore find the stochastic mean of the qubit state to be $\langle |\psi(t)\rangle \rangle = e^{i\phi_0} \langle e^{i\varphi(t)} \rangle |\psi(0)\rangle$, with the statistical phase accumulation [7]

$$\varphi(t) = \int_0^t dt' \omega(t'). \quad (\text{C3})$$

By assuming a zero-mean Gaussian distribution [28,30], the ensemble-averaged phase factor exponential becomes

$$\langle e^{i\varphi} \rangle = e^{-(\varphi^2)/2}. \quad (\text{C4})$$

Within the Gaussian approximation, the statistics of the system are entirely captured by second-order cumulants and we find from Eq. (C3) that the phase variance is

$$\langle \varphi^2 \rangle = \int_0^t dt_1 \int_0^t dt_2 \langle \omega(t_1) \omega(t_2) \rangle. \quad (\text{C5})$$

In a spin-echo experiment, the central π pulse effectively inverts the time evolution and we can express the phase accumulation as

$$\tilde{\varphi}(t) = \left(\int_0^{t/2} dt' - \int_{t/2}^t dt' \right) \omega(t'). \quad (\text{C6})$$

By using the definition of the noise PSD $S_\omega(\omega) = (1/2\pi) \int_{-\infty}^{\infty} d\tau e^{-i\omega\tau} \langle \omega(\tau) \omega(0) \rangle$ with stationary cumulant, the variance becomes

$$\begin{aligned} \langle \tilde{\varphi}^2 \rangle &= 4 \int_{-\infty}^{\infty} d\omega S_\omega(\omega) \left(\frac{\sin^2(\omega t/4)}{\omega/2} \right)^2 \\ &= 8 \int_0^{\infty} d\omega S_\omega(\omega) \left(\frac{\sin^2(\omega t/4)}{\omega/2} \right)^2. \end{aligned} \quad (\text{C7})$$

From Eq. (C4), we obtain the dephasing component for the spin-echo experiment

$$\langle e^{i\tilde{\varphi}} \rangle_E = \exp \left(-t^2 \int_0^\infty d\omega S_\omega(\omega) g_E(\omega, t) \right), \quad (\text{C8})$$

defining the filter function of the spin-echo experiment

$$g_E(\omega, t) = \left(\frac{\sin^2(\omega t/4)}{\omega t/4} \right)^2. \quad (\text{C9})$$

For a linear coupling of the noise source to the qubit, we can express the PSD in terms of flux Φ , $S_\omega(\omega) = (\partial\omega/\partial\Phi)^2 S_\Phi(\omega)$, and assume a $1/f$ scaling $S_\Phi(\omega) \equiv S(\omega) = A_\Phi/|\omega|$ to obtain

$$\langle e^{i\tilde{\varphi}} \rangle_E = \exp \left[-t^2 \left(\frac{\partial\omega}{\partial\Phi} \right)^2 A_\Phi \ln 2 \right]. \quad (\text{C10})$$

The dephasing component in the echo experiment therefore has Gaussian lineshape and we find a pure dephasing rate

$$\Gamma_\phi^E = \sqrt{A_\Phi \ln 2} \left| \frac{\partial\omega}{\partial\Phi} \right|. \quad (\text{C11})$$

In order to compare measured data with our model, we extract the measured flux variance with the inverse Fourier transform of the PSD at $\tau = 0$, weighted by the filter function $g_E(\omega, t)$ of the echo experiment for $t > 0$:

$$\begin{aligned} \langle \Phi^2 \rangle_{\text{inferred}} &= A_\Phi \int_{-\infty}^{\infty} \frac{d\omega}{|\omega|} g_E(\omega) \\ &= 2A_\Phi \int_0^\infty \frac{d\omega}{\omega} g_E(\omega) \\ &= 2A_\Phi \ln 2. \end{aligned} \quad (\text{C12})$$

APPENDIX D: FLUX NOISE MODEL BASED ON MAGNETIC DEFECTS

We assume noninteracting magnetic two-level system (TLS) defects distributed uniformly across the interfaces surrounding the SQUID, such as the aluminum-vacuum, silicon-vacuum, and silicon-aluminum interfaces. These TLS impurities are modeled as spins with magnetic moment m , each coupled to the SQUID through a flux mediated mutual inductance [14,15]. If some test current I_{SQ} in the SQUID creates a magnetic field \vec{B} at the location of a TLS, then the flux induced in the SQUID by this TLS is given by $\Phi_{\text{SQ}} = \vec{B} \cdot \vec{m}_{\text{TLS}}/I_{\text{SQ}}$. We will omit the indices in the following derivation for simplicity. Assuming a random angular distribution of TLS moments, we calculate

the total flux variance as

$$\langle \Phi^2 \rangle = \frac{1}{3} \sigma m^2 \int dA \left(\frac{B}{I} \right)^2, \quad (\text{D1})$$

where σ is the areal density of defects and the surface integral is taken over all considered SQUID interfaces. The factor $\frac{1}{3}$ comes from averaging over the random spin orientations.

The geometries for a toroidal SQUID and a circular SQUID with a rectangular cross section have been treated by Bialczak *et al.* [15]. For the SQUID geometry in our experiment—a rectangular SQUID with rectangular cross section—we find from Eq. (1) that

$$\langle \Phi^2 \rangle = \frac{1}{3} m^2 \sigma P \int dx \left(\frac{B(x)}{I} \right)^2, \quad (\text{D2})$$

where $P = 2X + 2Y + 4W$ is the SQUID perimeter with X , Y , and W being the SQUID dimensions as shown in Fig. 1 in the main text. The remaining integral, parameterized by x , is taken over the lengths of the considered interfaces perpendicular to the extension of the SQUID arms.

1. Analytic approximation

The analytic approximation of the model only considers the top surface of the SQUID as a host for magnetic defects, assuming an effectively two-dimensional film with $W \gg b$. In the integrals involved in this calculation, $x = 0$ is treated as the center of the SQUID wire and $x = \pm W/2$ correspond to its two edges. Assuming that the superconducting current flows only at the SQUID surface, the magnetic field at the surface is given by $B(x) = \mu_0 K(x)/2$, where $K(x)$ is the surface current density. We use a surface current density proportional to $1/\sqrt{1 - (2x/W)^2}$ [31] away from the edges, joined by an exponential near the edges at $x = \pm(W/2 - \lambda^2/2b)$. Enforcing that the current density has continuous slope, we obtain the following function for the current density along the width of the SQUID:

$$K(\bar{x}) = \begin{cases} K_0 \frac{1}{\sqrt{1 - (2\bar{x})^2}}, & |\bar{x}| \leq \frac{1 - \epsilon}{2}, \\ K_0 \sqrt{\frac{e}{2\epsilon}} \exp\left(\frac{|\bar{x}| - 1/2}{\epsilon}\right), & \frac{1 - \epsilon}{2} < |\bar{x}| \leq \frac{1}{2}. \end{cases} \quad (\text{D3})$$

Here $\bar{x} \equiv x/W$ and $\epsilon \equiv \lambda^2/bW$. Since $\epsilon \ll 1$, we keep only leading-order terms in ϵ . Evaluating Eq. (1) with this particular $B(x)$ and using the definition $I = \int dx K(x)$, we

obtain

$$\langle \Phi^2 \rangle = \frac{1}{3} \sigma m^2 P \left(\frac{\mu_0}{2} \right)^2 \frac{\int dx K(x)^2}{[\int dx K(x)]^2} \quad (\text{D4})$$

$$= \frac{\mu_0^2}{3\pi} m^2 \sigma \frac{P}{W} \left(\frac{\ln(2bW/\lambda^2)}{2\pi} + \frac{e-1}{2\pi} \right). \quad (\text{D5})$$

The important trends are that the flux variance, and therefore the flux noise power, increases linearly with the average perimeter P of the SQUID loop and decreases roughly inversely with its width W .

2. Numerical computation of the current distribution in a superconducting strip of finite thickness

We numerically compute the current distribution in a superconducting strip following the approach presented in Weeks *et al.* [42] and its extension by Sheen *et al.* [35]. It is based on the two-fluid model of superconductivity [36], where a complex conductivity accounts for both the resistive loss channel at nonzero frequencies (real part) as well as the kinetic energy of the supercurrent (imaginary part). The normal current is described by Ohm's law while the kinetic contribution is added through London's equation. The superconducting penetration depth λ enters via the complex conductivity.

We apply the method to calculate the current distribution in a single superconducting strip that is extended in the z direction and discretized into an appropriate number of parallel patches in the x - y plane; see Fig. 4. We extract the current distribution from the transmission line equation

$$\vec{I}(\omega) \propto -i\omega \hat{y} \vec{V}, \quad (\text{D6})$$

where all voltages are set to an identical value (unity). The admittance matrix \hat{y} is comprised of a resistive part and an inductive part, which in turn depend on the complex conductivity and partial inductances that contain the model geometry [42]. By dividing the currents I penetrating each patch by their cross-sectional area we readily find the volume current density $J(x, y)$ in the x - y plane.

Subsequently, we find the magnetic field $\vec{B}(x)$ on the surface of the strip (blue region in Fig. 4) with Biot-Savart's formula by integrating the current density $J(x, y)$ over the volume of the strip,

$$\vec{B}(\vec{r}) = \frac{\mu_0}{4\pi} \iiint_V dV \frac{J(x, y) \hat{z} \times \vec{r}'}{|\vec{r}'|^3}, \quad (\text{D7})$$

where \hat{z} denotes the unit vector along z and \vec{r}' is the vector from any point in the integration volume to the point where the field is being computed. The norm of this magnetic field, which is mainly directed along x except for some contribution along y close to the edges, enters our flux noise model Eq. (1), where it is integrated again along

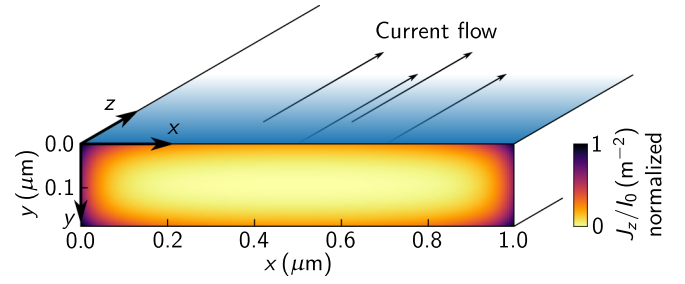


FIG. 4. Schematic drawing of a section of the SQUID loop in our experiment. Current is flowing along the z direction and we plot the numerically simulated current distribution J_z/I_0 at its cross section, normalized to a reference current I_0 . Simulation parameters are a standard design with wire width $W = 1 \mu\text{m}$ and film thickness $b = 190 \text{ nm}$. In order to compute the magnetic field on the surface of the strip (blue) that enters in the flux noise model Eq. (1), we use Biot-Savart's law.

the x dimension. The integrations are numerically approximated by Riemann sums. We chose different numerical discretizations in the successive integrations along x in order to exclude a systematic error and verified our numerical procedure by observing its convergence.

In Fig. 5 we show the results of the numerical simulations for different thickness regimes of the superconducting film forming the SQUID. For each thickness b , we plot the numerically obtained factor $\int dx B^2(x)/I^2$, a measure for the normalized magnetic field variance, versus the inverse wire width $1/W$. We show simulation results accounting for defect spins located only in the top surface of the SQUID (purple), and we also plot the numerical results taking into account all relevant interfaces (red), which are the top and bottom surfaces of the SQUID arms, their side faces, and the silicon-vacuum interfaces in the vicinity of the SQUID. The numerical simulation of the top surface can be directly compared to the analytic approximation, which yields, for the normalized magnetic field variance,

$$\int \frac{dx B^2(x)}{I^2} = \frac{\mu_0^2}{\pi W} \left(\frac{\ln(2bW/\lambda^2)}{2\pi} + \frac{e-1}{2\pi} \right); \quad (\text{D8})$$

see Sec. D 1.

We first verify our numerical approach by comparing simulation results for a thin strip with $b = 20 \text{ nm}$ to the result obtained with the approximate formula; see Fig. 5(a). For large wire widths $W \gg b, \lambda$ in particular, the approximation of the analytic formula is valid and it matches the numerical result for considering defect spins only in the top surface. For thin films, the numerical result recovers the expected linear dependence of $\int dx B^2(x)/I^2$ on $1/W$ to first order. Small deviations for smaller W reveal the limitation of the approximate formula [31]. For the film thickness $b = 190 \text{ nm}$ used in our experiment [see Fig. 5(b)], the numerical result and the analytic approximation diverge even for large W since the condition $b \sim \lambda$

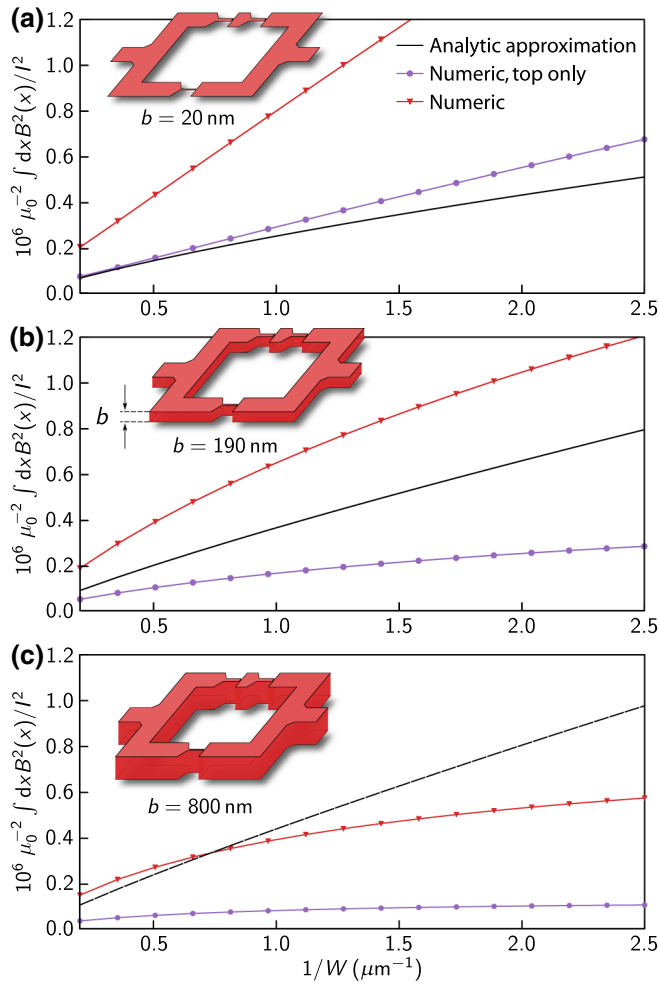


FIG. 5. Numerical simulation results for various film thicknesses b . We plot the numerical value $\mu_0^{-2} \int dx B^2(x)/I^2$ that enters the model for magnetic flux noise in Eq. (1), replacing the analytic approximation. The purple lines and circles show the results when considering only the top surface of the SQUID and the red lines with triangles show the result for both the top surface and the side faces summed. The analytic approximation is given as a black line. (a) Results for a very thin aluminum thickness $b = 20$ nm, where the numerical simulation agrees with the analytic formula for $W \gg b, \lambda$. (b) Results for the thickness $b = 190$ nm, as used in our experiment. (c) The analytic expression breaks down entirely for a thick film with $b = 800$ nm, while the numerical result indicates a reduced noise sensitivity as compared to smaller wire thicknesses.

is violated. For an even larger thickness of $b = 800$ nm, the analytic approximation breaks down completely; see Fig. 5(c). Remarkably, we find that increasing the film thickness b reduces the noise amplitude considerably, an effect analogous to the reduction in noise with increasing wire width W . We want to point out that the contribution from the side faces of the SQUID vanishes in the limit of $b \rightarrow 0$ [see Fig. 5(a)].

APPENDIX E: EXTENDED DATA SET

As discussed previously, the double angle shadow evaporation technique creates an increased width along the vertical arms of the SQUIDs by approximately 350 nm. In SQUIDs with aspect ratios $X \ll Y$ in particular, this effect results in an average effective width significantly different from the nominal value of $1 \mu\text{m}$. In Fig. 3(a) in the main text, we therefore omitted data points for SQUIDs containing these smallest aspect ratios for clarity. Here in Fig. 6, we show our complete data set, where data points in light blue correspond to SQUIDs with constant X but the vertical dimension Y of the SQUID variably increased. Apart from the slight decrease of the measured $\sqrt{A_\Phi}$ due to the increased width, the expected linear scaling of the theory is well reproduced in this extended parameter range.

APPENDIX F: GROUND PLANE PERFORATIONS

We use chip designs for this noise study with $3 \mu\text{m} \times 3 \mu\text{m}$ sized ground plane perforations acting as flux traps, distributed at a pitch of $13 \mu\text{m}$ (center-to-center distance). We do not observe a dependence of the flux noise amplitudes on the presence or absence of ground plane perforations. During the course of this experiment, we noted flux instabilities on a timescale of seconds and nonlinear flux tuning for bias currents below approximately 1 mA, but stable conditions for larger bias currents. In order to operate in the stable regime, we chose optimal bias points corresponding to larger bias currents to perform the flux noise study. We speculate that this behavior is caused by a reconfiguration of weakly pinned flux vortices.

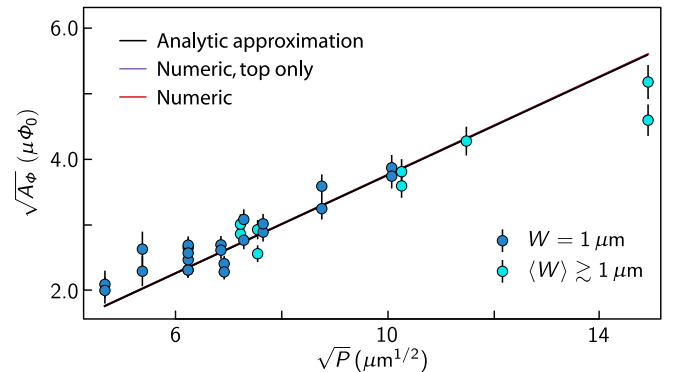


FIG. 6. Extended data set of measured flux noise amplitudes $\sqrt{A_\Phi}$ in dependence of SQUID perimeter P for a nominally constant wire width $W = 1 \mu\text{m}$. Dark blue data points are reproduced from Fig. 3(a) in the main text. Light blue data points represent nine additional SQUIDs from a chip with varied aspect ratios (X/Y). As a result of the shadow angle evaporation technique, the effective width for data points with small aspect ratios is increased, yielding a reduction of flux noise. The fits shown take into account all data points and the resulting surface spin densities are within 10% of the respective values extracted from the fits in Fig. 3.

- [1] M. H. Devoret and R. J. Schoelkopf, Superconducting circuits for quantum information: An outlook, *Science* **339**, 1169 (2013).
- [2] M. Kjaergaard, M. E. Schwartz, J. Braumüller, P. Krantz, J. I.-J. Wang, S. Gustavsson, and W. D. Oliver, Superconducting qubits: Current state of play, *Annu. Rev. Condens. Matter Phys.* **11**, 369 (2020).
- [3] S. Boixo, S. V. Isakov, V. N. Smelyanskiy, R. Babbush, N. Ding, Z. Jiang, M. J. Bremner, J. M. Martinis, and H. Neven, Characterizing quantum supremacy in near-term devices, *Nat. Phys.* **14**, 595 (2018).
- [4] F. Arute *et al.*, Quantum supremacy using a programmable superconducting processor, *Nature* **574**, 505 (2019).
- [5] W. D. Oliver and P. B. Welander, Materials in superconducting quantum bits, *MRS Bull.* **38**, 816 (2013).
- [6] R. Barends, J. Kelly, A. Megrant, D. Sank, E. Jeffrey, Y. Chen, Y. Yin, B. Chiaro, J. Mutus, C. Neill, P. O'Malley, P. Roushan, J. Wenner, T. C. White, A. N. Cleland, and J. M. Martinis, Coherent Josephson Qubit Suitable for Scalable Quantum Integrated Circuits, *Phys. Rev. Lett.* **111**, 080502 (2013).
- [7] E. Paladino, Y. M. Galperin, G. Falci, and B. L. Altshuler, $1/f$ noise: Implications for solid-state quantum information, *Rev. Mod. Phys.* **86**, 361 (2014).
- [8] P. Dutta and P. M. Horn, Low-frequency fluctuations in solids: $1/f$ noise, *Rev. Mod. Phys.* **53**, 497 (1981).
- [9] R. H. Koch, J. Clarke, W. M. Goubau, J. M. Martinis, C. M. Pegrum, and D. J. van Harlingen, Flicker ($1/f$) noise in tunnel junction dc squids, *J. Low Temp. Phys.* **51**, 207 (1983).
- [10] F. C. Wellstood, C. Urbina, and J. Clarke, Low-frequency noise in dc superconducting quantum interference devices below 1 K, *Appl. Phys. Lett.* **50**, 772 (1987).
- [11] G. Ithier, E. Collin, P. Joyez, P. J. Meeson, D. Vion, D. Esteve, F. Chiarello, A. Shnirman, Y. Makhlin, J. Schrieffer, and G. Schön, Decoherence in a superconducting quantum bit circuit, *Phys. Rev. B* **72**, 134519 (2005).
- [12] F. Yoshihara, K. Harrabi, A. O. Niskanen, Y. Nakamura, and J. S. Tsai, Decoherence of Flux Qubits due to $1/f$ Flux Noise, *Phys. Rev. Lett.* **97**, 167001 (2006).
- [13] K. Kakuyanagi, T. Meno, S. Saito, H. Nakano, K. Semba, H. Takayanagi, F. Deppe, and A. Shnirman, Dephasing of a Superconducting Flux Qubit, *Phys. Rev. Lett.* **98**, 047004 (2007).
- [14] R. H. Koch, D. P. DiVincenzo, and J. Clarke, Model for $1/f$ Flux Noise in Squids and Qubits, *Phys. Rev. Lett.* **98**, 267003 (2007).
- [15] R. C. Bialczak, R. McDermott, M. Ansmann, M. Hofheinz, N. Katz, E. Lucero, M. Neeley, A. D. O'Connell, H. Wang, A. N. Cleland, and J. M. Martinis, $1/f$ Flux Noise in Josephson Phase Qubits, *Phys. Rev. Lett.* **99**, 187006 (2007).
- [16] S. Gustavsson, J. Bylander, F. Yan, W. D. Oliver, F. Yoshihara, and Y. Nakamura, Noise correlations in a flux qubit with tunable tunnel coupling, *Phys. Rev. B* **84**, 014525 (2011).
- [17] D. Sank *et al.*, Flux Noise Probed with Real Time Qubit Tomography in a Josephson Phase Qubit, *Phys. Rev. Lett.* **109**, 067001 (2012).
- [18] F. Yan, J. Bylander, S. Gustavsson, F. Yoshihara, K. Harrabi, D. G. Cory, T. P. Orlando, Y. Nakamura, J.-S. Tsai, and W. D. Oliver, Spectroscopy of low-frequency noise and its temperature dependence in a superconducting qubit, *Phys. Rev. B* **85**, 174521 (2012).
- [19] F. Yan, S. Gustavsson, J. Bylander, X. Jin, F. Yoshihara, D. G. Cory, Y. Nakamura, T. P. Orlando, and W. D. Oliver, Rotating-frame relaxation as a noise spectrum analyser of a superconducting qubit undergoing driven evolution, *Nat. Commun.* **4**, 2337 (2013).
- [20] P. Krantz, M. Kjaergaard, F. Yan, T. P. Orlando, S. Gustavsson, and W. D. Oliver, A quantum engineer's guide to superconducting qubits, *Appl. Phys. Rev.* **6**, 021318 (2019).
- [21] F. Yan, S. Gustavsson, A. Kamal, J. Birenbaum, A. P. Sears, D. Hover, T. J. Gudmundsen, D. Rosenberg, G. Samach, S. Weber, J. L. Yoder, T. P. Orlando, J. Clarke, A. J. Kerman, and W. D. Oliver, The flux qubit revisited to enhance coherence and reproducibility, *Nat. Commun.* **7**, 12964 (2016).
- [22] C. M. Quintana *et al.*, Observation of Classical-Quantum Crossover of $1/f$ Flux Noise and its Paramagnetic Temperature Dependence, *Phys. Rev. Lett.* **118**, 057702 (2017).
- [23] H. Wang, C. Shi, J. Hu, S. Han, C. C. Yu, and R. Q. Wu, Candidate Source of Flux Noise in SQUIDS: Adsorbed Oxygen Molecules, *Phys. Rev. Lett.* **115**, 077002 (2015).
- [24] P. Kumar, S. Sendelbach, M. A. Beck, J. W. Freeland, Z. Wang, H. Wang, C. C. Yu, R. Q. Wu, D. P. Pappas, and R. McDermott, Origin and Reduction of $1/f$ Magnetic Flux Noise in Superconducting Devices, *Phys. Rev. Appl.* **6**, 041001 (2016).
- [25] T. Lanting, A. J. Berkley, B. Bumble, P. Bunyk, A. Fung, J. Johansson, A. Kaul, A. Kleinsasser, E. Ladizinsky, F. Maibaum, R. Harris, M. W. Johnson, E. Tolkacheva, and M. H. S. Amin, Geometrical dependence of the low-frequency noise in superconducting flux qubits, *Phys. Rev. B* **79**, 060509(R) (2009).
- [26] S. Sendelbach, D. Hover, A. Kittel, M. Mück, J. M. Martinis, and R. McDermott, Magnetism in SQUIDS at Millikelvin Temperatures, *Phys. Rev. Lett.* **100**, 227006 (2008).
- [27] S. M. Anton, J. S. Birenbaum, S. R. O'Kelley, V. Bolkhovskoy, D. A. Braje, G. Fitch, M. Neeley, G. C. Hilton, H.-M. Cho, K. D. Irwin, F. C. Wellstood, W. D. Oliver, A. Shnirman, and J. Clarke, Magnetic Flux Noise in dc SQUIDS: Temperature and Geometry Dependence, *Phys. Rev. Lett.* **110**, 147002 (2013).
- [28] Y. Makhlin and A. Shnirman, Dephasing of Solid-State Qubits at Optimal Points, *Phys. Rev. Lett.* **92**, 178301 (2004).
- [29] J. Bylander, S. Gustavsson, F. Yan, F. Yoshihara, K. Harrabi, G. Fitch, D. G. Cory, Y. Nakamura, J.-S. Tsai, and W. D. Oliver, Noise spectroscopy through dynamical decoupling with a superconducting flux qubit, *Nat. Phys.* **7**, 565 (2011).
- [30] G. Ithier, Ph.D. thesis, Quantronics group, Saclay, 2005.
- [31] E. Roderick and E. Wilson, Current distribution in thin superconducting films, *Nature* **194**, 1167 (1962).
- [32] The current distribution across the width of the SQUID arms only enters the flux noise amplitude through the factor $\int dx K(x)^2 / (\int dx K(x))^2$. Minimizing this expression yields

- that a uniform current distribution $K(x) = \text{const.}$ minimizes flux noise.
- [33] T. Van Duzer and C. W. Turner, *Principles of Superconductive Devices and Circuits* (Elsevier, New York, 1981).
- [34] C. Poole, H. Farach, and R. Creswick, *Superconductivity* (Elsevier Science, Burlington, 2013).
- [35] D. M. Sheen, S. M. Ali, D. E. Oates, R. A. Withers, and J. A. Kong, Current distribution, resistance, and inductance for superconducting strip transmission lines, *IEEE Trans. Appl. Supercond.* **1**, 108 (1991).
- [36] M. Tinkham, *Introduction to Superconductivity* (Dover, New York, 2004), 2nd ed.
- [37] W. Woods, G. Calusine, A. Melville, A. Sevi, E. Golden, D. K. Kim, D. Rosenberg, J. L. Yoder, and W. D. Oliver, Determining Interface Dielectric Losses in Superconducting Coplanar-Waveguide Resonators, *Phys. Rev. Appl.* **12**, 014012 (2019).
- [38] J. M. Martinis, K. B. Cooper, R. McDermott, M. Steffen, M. Ansmann, K. D. Osborn, K. Cicak, S. Oh, D. P. Pappas, R. W. Simmonds, and C. C. Yu, Decoherence in Josephson Qubits from Dielectric Loss, *Phys. Rev. Lett.* **95**, 210503 (2005).
- [39] See Supplemental Material at <http://link.aps.org/supplemental/10.1103/PhysRevApplied.13.054079> for a data summary.
- [40] G. J. Dolan, Offset masks for lift-off photoprocessing, *Appl. Phys. Lett.* **31**, 337 (1977).
- [41] J. Lisenfeld, A. Bilmes, A. Megrant, R. Barends, J. Kelly, P. Klimov, G. Weiss, J. M. Martinis, and A. V. Ustinov, Electric field spectroscopy of material defects in transmon qubits, *npj Quantum Inf.* **5**, 105 (2019).
- [42] W. T. Weeks, L. L. Wu, M. F. McAllister, and A. Singh, Resistive and inductive skin effect in rectangular conductors, *IBM J. Res. Dev.* **23**, 652 (1979).